Flux Weakening Surface Mounted Permanent Magnet Servo Motor Design with Enhanced Self-Sensing Properties

Huthaifa Mohammad Flieh, Timothy Slininger, Robert D. Lorenz
University of Wisconsin-Madison, WEMPEC
Madison, Wisconsin, USA
hflieh@wisc.edu, t.slininger@wisc.edu, rdlorenz@wisc.edu

Shao-Chuan Chien, Li-Hsing Ku
Motor Drive Solution BU, Delta Electronics, Inc
Taiwan
sean.chien@deltaww.com, rick.ku@deltaww.com

Abstract— Servo motors are widely used in automation and robots. These motors achieve high dynamic performance with precise motion control. Flux weakening surface mounted permanent magnet synchronous motors (FW-SPMSMs) are the main type used in servos due to high peak torque allowing high acceleration rates, and low cogging and ripple torques allowing smooth and precise motion control. Standard FW-SPMSMs are not suitable for injection-based self-sensing control. Many techniques have been reported in the literature to design slightly salient SPMSMs. However, the reported techniques are not suitable for servo applications due to the loss of motor saliency with load or the techniques might affect the motor power conversion through degrading the peak, cogging, or ripple torques. This paper will present a new methodology for the design of high-performance FW-SPMSMs for servo applications with enhanced self-sensing properties without degrading motor power conversion. The designed motor saliency improves with load leading to enhancement of self-sensing performance.

Keywords—FW, FI, SPMSM, Injection-based self-sensing, sensorless , saliency

I. INTRODUCTION

Flux weakening surface mounted permanent magnet motors (FW-SPMSMs) –which are usually called SPMSMs- are one of the main types of motors used in servo applications due to the high peak torque performance which reflects a high acceleration rate and very low levels of cogging and ripple torques, leading to smooth and precise speed and position control. Servos typically achieve a high acceleration rate by applying double or triple the rated torque for a short period.

Self-sensing techniques allow for control of the motor without a position sensor by using the motor itself as a sensor. This will improve the reliability of the drive, where no position sensors with long cables are needed, and will reduce the size and cost of the motor by removing the position sensor. Self-sensing techniques can be classified into two main categories. Motor back-EMF tracking, which is an effective technique for controlling the motor at medium and high-speed operation, and is effective for any kind of electromagnetic motors. However, this technique fails at zero-to-low speed operation due to poor signal-to-noise ratio in the estimated back-EMF, caused by inverter nonlinearity and deadtime effect [1]. The other self-sensing methods are injection-based self-sensing techniques, which is effective to control the motor at zero and low speed operation.

This research is sponsored by Delta Electronics, Inc. Taiwan

Injection-based self-sensing techniques have been widely investigated by many researchers. These techniques are used to control the motor at zero and low-speed operation through tracking motor saliency. These techniques require a salient motor like an interior permanent magnet synchronous motor (IPMSM) [2], [3].

Standard SPMSMs are non-salient motors and can't be used with saliency-based (injection based) self-sensing techniques. Several techniques were reported in the literature to enhance the self-sensing properties for SPMSMs by creating small detectable saliency. For example, in [4] the authors propose using a ringed pole SPMSM structure, creating a small saliency by the additional mutual inductance between the d-axis winding and the copper ring. The designed SPMSM uses a ringed magnet leading to a trapezoidal back-EMF and can't be used in servo applications that require very low ripple and cogging torques. The authors of [5] proposed designing an SPMSM with a narrow tooth tip utilizing the zigzag leakage flux, which creates a small saliency. The designed motor also uses a ringed type magnet and cannot be used in servo applications. In [6] the authors showed that inset type SPMSMs have a trackable saliency. However, this design has lower peak torque compared to a standard FW-SPMSMs due to the additional leakage flux in the added iron between the magnets.

The saliency ratio decreases with increasing the load torque for standard flux weakening PMSM, due to saturation of the q-axis flux path with motor current. This leads to decreased q-axis inductance, while d-axis inductance remains at the same level. For some designs, the motor loses its saliency completely even at a torque level lower than rated torque, preventing use of injection-based self-sensing techniques at that torque level. In [7], the authors proposed modifying the injection angle when the motor loses its saliency, allowing the use of self-sensing techniques at this operating point, but with an extra torque ripple to the motor which is not acceptable for servo motors. It is necessary for the designed servo motor to maintain sufficient saliency ratio even at two or three times the rated torque, allowing the control of motor using self-sensing techniques during rapid servo operation.

In [8], a flux intensifying SPMSM (FI-SPMSM) for servo applications is proposed, the designed motor uses less magnet material compared to FW-SPMSMs while achieving very low ripple and cogging torques through use of bread loaf magnets. This design maintains a small saliency even at twice the rated torque, enabling self-sensing control of the motor during rapid servo acceleration as reported in [9]. However, this design

achieves lower peak torque compared to standard FW-SPMSMs, which might not be acceptable for some servo applications.

This paper proposes a methodology to design FW-SPMSMs with enhanced self-sensing properties without degrading the power conversion properties of the motor this achieves high peak torque, low cogging and ripple torques, and maintains a trackable saliency even at twice the rated torque. Section II of this paper will identify the main design parameters that impact the motor self-sensing properties, while section III of the paper will show optimization of the defined parameters for the final motor design. Experimental evaluation of the fabricated motor, including self-sensing control performance, will be presented in section IV Finally, conclusions about this paper will be summarized in section V.

II. FW-SPMSM Servo Motor Design: Key Variables for Enhanced Self-Sensing Properties

The initial design parameters were calculated by solving the general SPMSM sizing equations found in [10]–[13]. A 24-slot and 8-pole full pitch distributed winding configuration is selected to achieve very low cogging torque [12]. A bread-loaf magnet with a parallel magnetization pattern is selected to shape the airgap flux and to achieve sinusoidal back-EMF with very low cogging and ripple torques [14]. Table I summarizes the main characteristics and dimensions of the designed SPMSM. Figure 1 shows the designed stator.

TABLE I. SPMSM motor specifications

Specification	Value	Specification	Value
Rated power	3.7 kW	Stator inner diameter	70 mm
Rated torque	17.5 Nm	Stator outer diameter	130 mm
Rated speed	2000 r/min	Max speed	4000 r/min
Number of poles	8	Number of slots	24
Airgap length	1.1 mm	Peak torque	43 NM
Stack length	94 mm	Cogging / ripple torque	≤ 0.5% / 2%

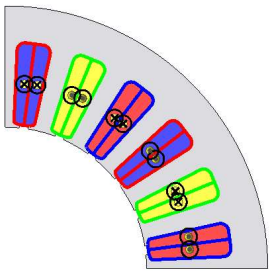

Fig. 1 The designed stator with 24 slots

The key design variables that impact the self-sensing properties are identified in this section. The tradeoff between self-sensing and power conversion performance are investigated using 2D FEA with JMAG™ Designer software.

A. Magnet Shape

To achieve very low cogging and ripple torque performance, the magnet needs to be shaped to achieve a sinusoidal back-EMF with low airgap harmonics. Bread loaf or arc shape magnets can be used. To realize the impact of magnet shape on the motor self-sensing properties, three rotors were designed using arc, bread loaf, and thick bread loaf magnets. Figure 2 shows the designed rotors.

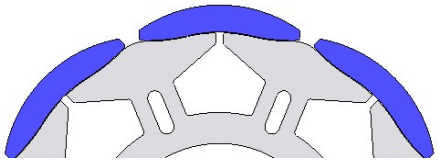

(a) Rotor using arc shape magnet

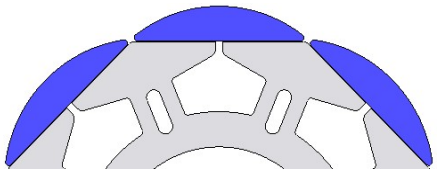

(b) Rotor using bread loaf magnet

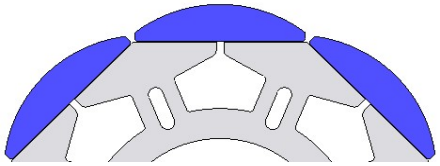

(c) Rotor using thick bread loaf magnet

Fig. 2 The designed rotors using different magnet shapes

Figure 3 shows the saliency ratio variation with motor torque (with respect to q-axis current while d-axis current is controlled at zero), while Fig.4 shows the inductance variation with load using different magnet shapes. The designed rotor with bread loaf magnets has similar q-axis inductance to the one with arc magnets. Bread loaf magnets are thicker in the center where the d-axis flux paths pass leading to lower d-axis inductance with increasing the saliency ratio by a factor of 2. Further increases in the bread loaf magnet thickness leads to lower d-axis inductance, however, the q-axis inductance will also slightly decrease due to increasing the magnet edge thickness where the q-axis flux path passes leading to a small enhancement in the motor saliency as can be seen in Fig.3.

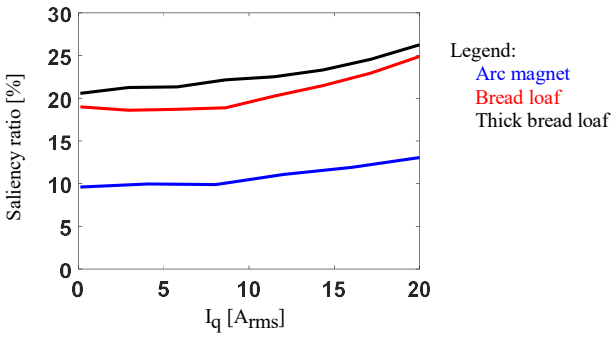

Fig. 3 Motor saliency ratio variation with load current using different magnet shapes

In general, bread-loaf magnets are easier to manufacture. The thickness of the magnet typically is selected to avoid magnet demagnetization at the worst operating condition.

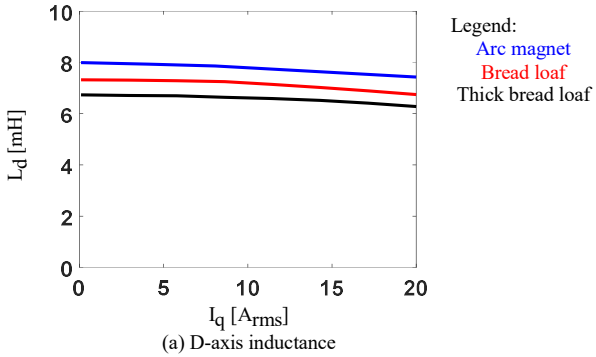

(a) D-axis inductance

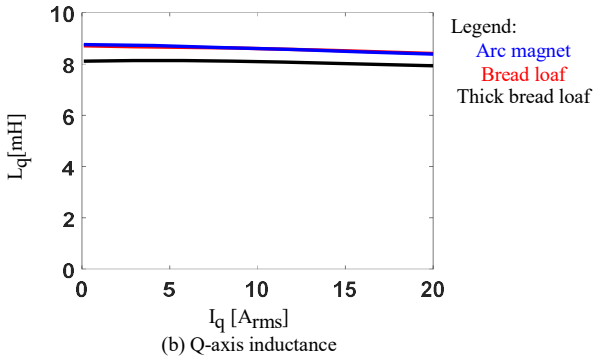

(b) Q-axis inductance

Fig. 4 Motor inductance variation with load current using different magnet shapes

B. *Iron Notches*

Adding small iron notches between adjacent magnets leads to a slight increase of the leakage flux with a small reduction of motor airgap flux linkage and average torque. However, these iron notches will decrease the reluctance in the q-axis flux path, increasing the q-axis inductance without affecting the d-axis inductance, which enhances the motor saliency ratio. Figure 5 shows the designed rotors with and without iron notches. The rotor without the notches produces 17.78 Nm torque while the torque after the iron notches slightly decreased to 17.737 Nm. However, motor saliency ratio improved by 80% as can be seen in Fig.6-c.

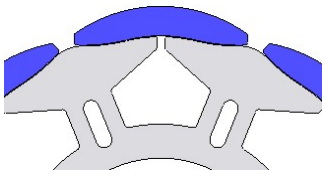

(a) Rotor without iron notch

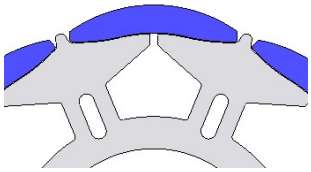

(b) Rotor with iron notch

Fig. 5 The designed rotors with and without iron notches

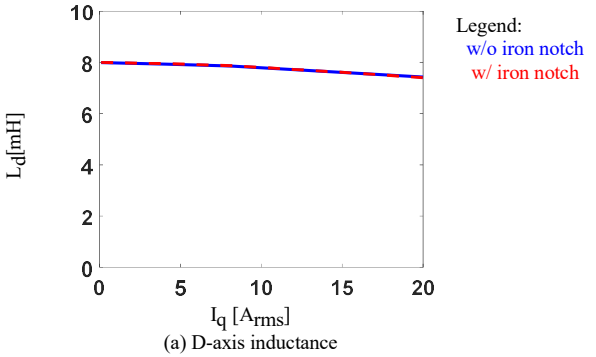

(a) D-axis inductance

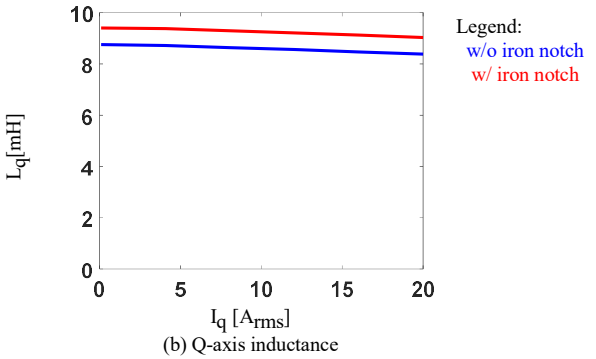

(b) Q-axis inductance

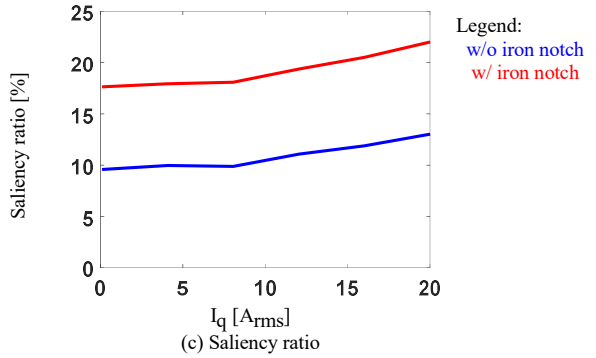

(c) Saliency ratio

Fig. 6 Motor inductance and saliency ratio Vs load current using rotors with and without iron notches

C. *D-axis Flux Barriers*

Q-axis flux barriers were proposed with FI-SPMSMs in [8], these barriers were used to decrease q-axis inductance and were effective with flux intensifying motors. However, this kind of barriers is not effective with FW-SPMSMs. In this paper, d-axis flux barriers are proposed. These barriers can be used to shape the flux path in the d-axis. The d-axis inductance can be decreased by slightly saturating the rotor d-axis flux path, enhancing motor saliency. However, this might slightly decrease motor torque production.

The impact of the flux barrier size on motor saliency ratio and power conversion is evaluated using 2D-FEA. The flux barrier size is varied by varying the flux barrier angle as in Fig.7. Selecting a small flux barrier angle leads to small size barriers, with minimal impact on the motor saliency ratio. However, increasing the flux barrier angle leads to increased barrier size, saturating the d-axis flux path in the rotor and decreasing the d-

axis inductance which enhances the motor saliency ratio. However, this will impact average motor torque, as can be seen from Fig.8.

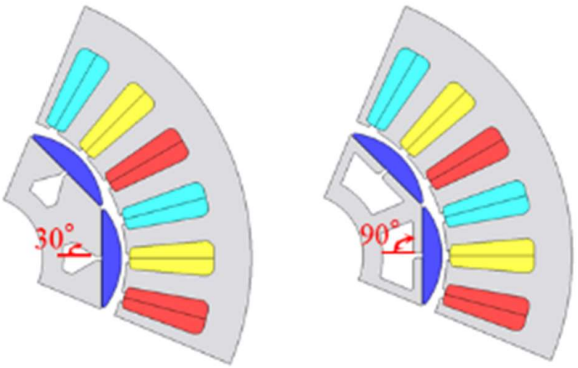

(a) Rotor with small d axis flux barriers (b) Rotor with large d-axis flux barriers

Fig. 7 The designed rotors using different d-axis flux barrier size

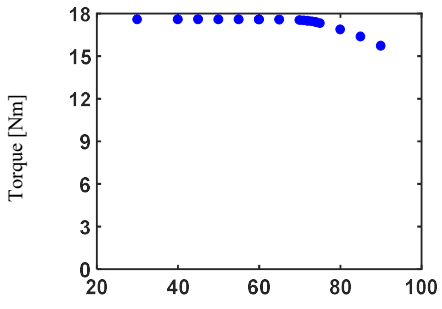

(a) D-axis inductance

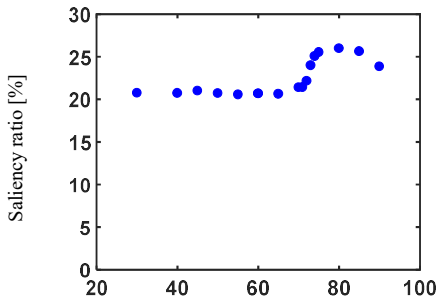

(b) Q-axis inductance

Fig. 8 Impact of the d-axis flux barriers on motor power conversion and self-sensing properties

D. Motor Stack Length

FW-SMPSM torque is linearly proportional to the stack length. Increasing the stack length will lead to increased motor torque and size. This parameter can be adjusted to get the desired output torque from the designed motor. For example, decreasing the motor stack length will decrease the inductance in both the d and q axes, leading to a fixed motor saliency ratio as in Fig.9-a. However, the spatial information extracted through high-frequency signal injection can be calculated using (1) and will be improved, achieving a better signal-to-noise ratio ($\Delta L/(L_d*L_q)$) [2] as shown in Fig. 9-b.

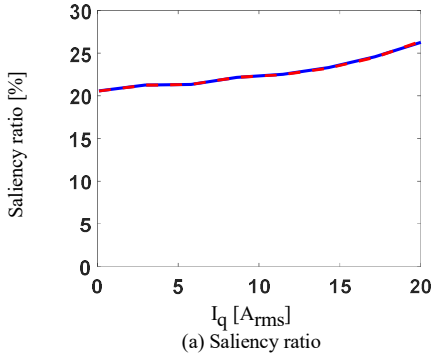

(a) Saliency ratio

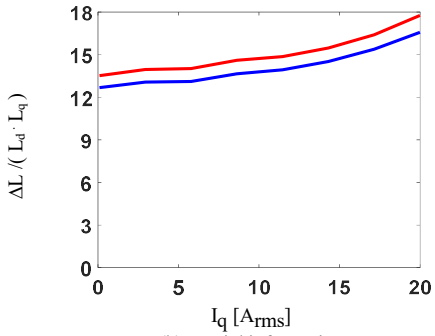

(b) Spatial information

Fig. 9 Impact of motor stack length on the motor self-sensing properties

$$\varepsilon_f \approx \frac{-V_{inj}}{2\omega_c} \bullet \frac{\Delta L}{L_d\ L_q} \bullet \theta_{err} \qquad (1)$$

where:

V_{inj} = amplitude of the injected high-frequency d-axis voltage [volt],

Ld, Lq = d, q inductance [H],

$\Delta L = (Ld - Lq)/2$ [H],

ω_c = the injected voltage signal frequency [rad/sec],

θerr= position error [rad],

ε_f = Extracted position error from current demodulation [rad].

III. FW-SPMSM Servo Motor Design Methodology with Enhanced Self-Sensing Properties

In the previous section, the key design variables that impact motor self-sensing properties were identified. The tradeoff between self-sensing and power conversion properties were also evaluated in the previous section. The key design variables need to be optimized simultaneously to obtain a good design with enhanced self-sensing without degrading motor power conversion. Motor stack length is not included in the optimization process (set to 1 pu), this parameter is adjusted in the optimized design to get the desired torque.

In this section, multi-objective optimization using JMAG™ Designer software is performed. A bread loaf magnet shape is used due to a lower manufacturing cost compared to arc shape magnets. Table II summarizes the parameters varied during the optimization process. This table also shows the set objective functions. Figure 10 shows the optimized motor rotor with the varied parameters marked. The magnet thickness is selected to avoid partial demagnetization at 3 pu current and at 120˚ C.

TABLE II. Multi objective optimization variables and objective functions

Optimization variable	Range	Objective function	Value
Magnet span (P1)	21-23 mm	Torque ripple	≤ 2%
Magnet arc (P2)	18-22 mm	Cogging Torque	≤ 0.5%
Flux path thickness (P3)	0.6-1.4 mm	Average torque	Maximize
Flux barrier angle (P4)	60-85 deg	Saliency ratio	Maximize
Iron notch radius (P5)	0.2-0.6 mm	Magnet volume	minimize

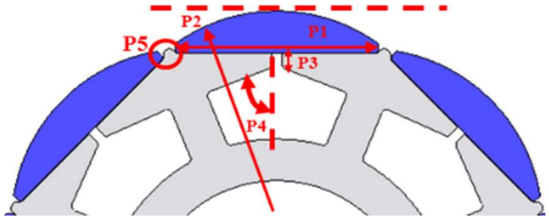

Fig. 10 The optimized rotor with key variables marked

Figure 11-a shows the optimized design, while Fig.11-b shows the fabricated rotor. Table III summarizes the main characteristics of the optimized motor design. This motor achieves the desired average, ripple and cogging torque requirements for servo application.

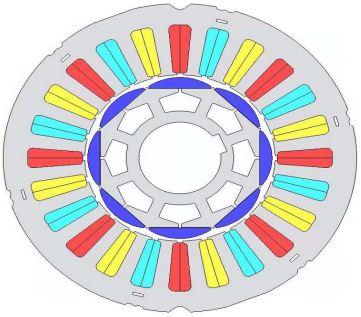

(a) The optimized design

(b) The fabricated rotor

Fig. 11 The optimized motor design and the fabricated rotor prototype

TABLE III. The optimized motor characteristics

Physical quantity	Value
Torque ripple	0.321 Nm(1.8%)
Cogging Torque	0.0636 Nm(0.36%)
Average torque @ 6.8 A_{rms}	17.742 Nm
Saliency ratio @ no load	26%
Saliency ratio @ 2 pu load	33%
Stack length	89 mm

The phase back-EMF for the optimized design is calculated using 2D-FEA and is shown in Fig.12, while the average motor torque at the rated current is shown in Fig.13-a. The motor cogging torque is shown in Fig 13-b. The optimized design motor achieves the servo requirements with 0.36% cogging torque and 1.8% torque ripple compared to the rated torque.

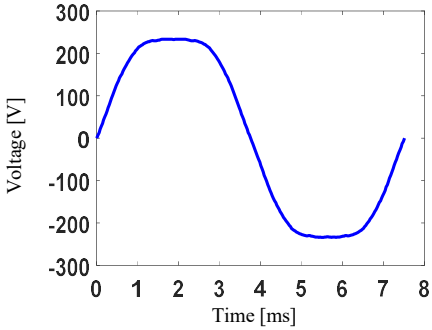

Fig. 12 Simulated motor back-EMF using 2D-FEA

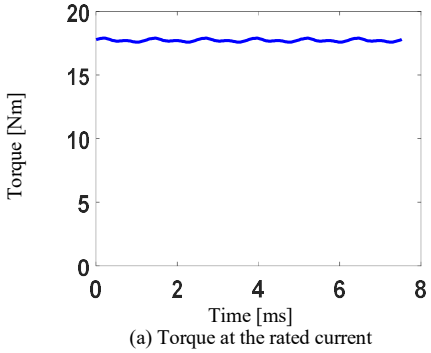

(a) Torque at the rated current

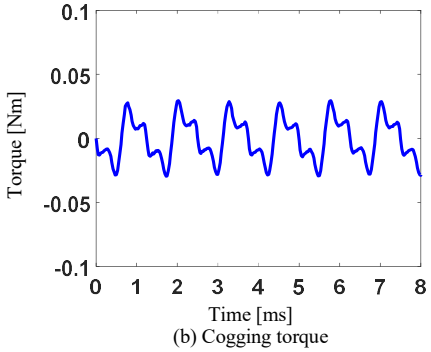

(b) Cogging torque

Fig. 13 Simulated optimized motor average and ripple torque

Figure 14-a shows the calculated d and q axis inductances with load condition for the optimized motor. Using d-axis flux barriers leads to relatively fixed q-axis inductance which is not affected by the motor load (q-axis current), through using the d-axis flux to uniformly saturate the q-axis flux path around the magnet edge. The d-axis inductance is slightly decreased with the q-axis current due to iron saturation leading to an enhancement in motor saliency ratio with load condition by 27% as can be seen from Fig.14-b.

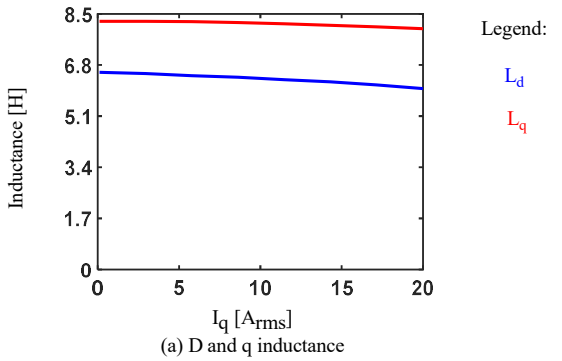

(a) D and q inductance

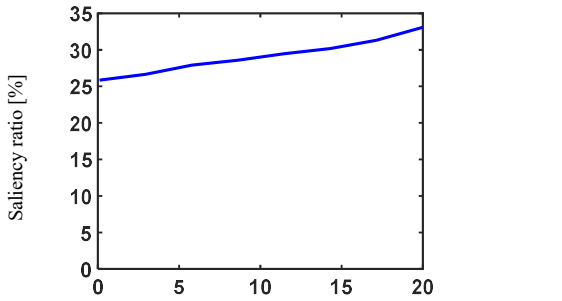

(b) Saliency ratio

Fig. 14 The optimized motor design inductance and saliency ratio variation with load current

IV. Experimental Evaluation of the Designed FW-SPMSM Servo Motor

The optimized design motor was fabricated and evaluated experimentally by connecting it to a 7 KW load motor as in Fig.15.

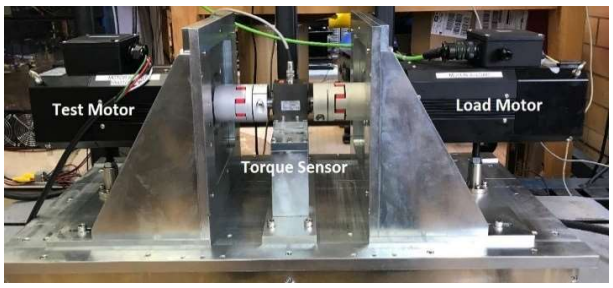

Fig. 15 The testing dynamometer

The load motor was controlled to spin the dynamometer at 2000 r/min. Then the line-line back-EMF voltage for the designed motor was measured using a differential voltage probe. The measured EMF value is 3.75% lower than the calculated one from 2D-FEA as in Fig.16-a. This is due to not modeling the end winding effect and leakage flux. This motor achieves smaller secondary harmonics than expected as in Fig.16-b which indicates low cogging torque.

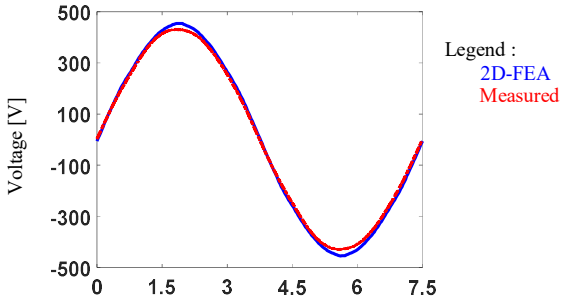

(a) Line back-EMF @ 2000 r/min

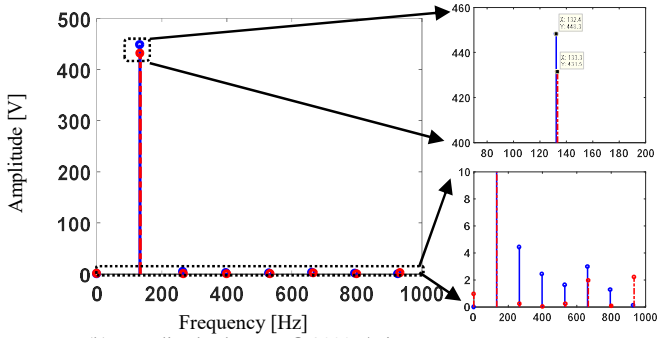

(b) FFT- line back-EMF @ 2000 r/min

Fig. 16 Comparsion between the measured line back-EMF and estimated EMF using 2D-FEA at 2000 r/min for the designed motor

Next, the motor d-q inductance variation with load (q-axis current) is measured and compared with the expected value from FEA. 3D-FEA is performed to estimate the motor leakage inductance which is then added to the calculated inductance values from 2D-FEA as described in [8]. The motor inductance is measured through locking the rotor and injecting a high-frequency chirp voltage signal to the dq frame. Then the inductance values are calculated from the current response at different q-axis levels (different torque levels). Figure 17 compares the measured d,q inductance values with calculated values using FEA at different torque levels (different q-axis current) while controlling d-axis current to be zero. The measured valued is in good agreement with the expected values from FEA.

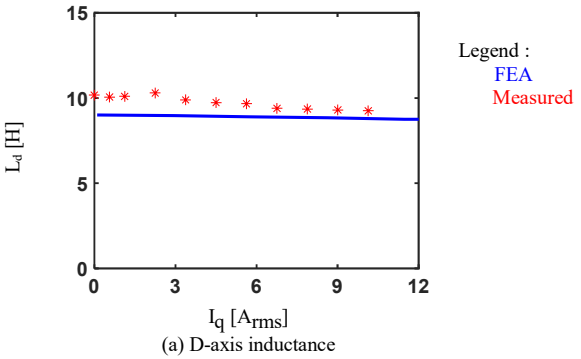

(a) D-axis inductance

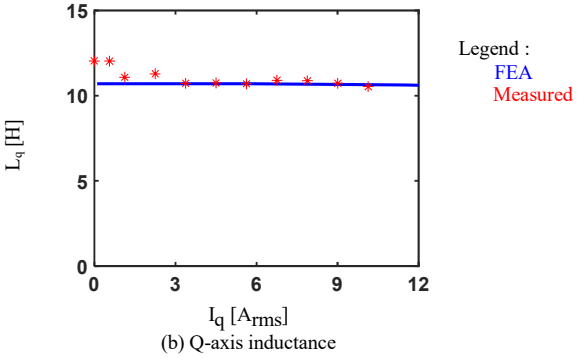

(b) Q-axis inductance

Fig. 17 Measured and simulated inductance variation with load current (I_d=0) for the designed motor

The designed motor is then controlled using high-frequency flux injection (HFFI) self-sensing with DB-DTFC as described in [9]. The block diagram of this control structure is shown in Fig.18.

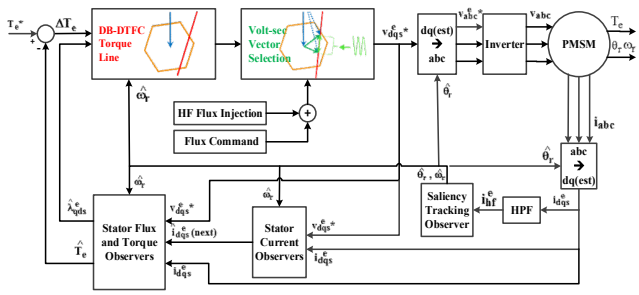

Fig. 18 High frequency flux injection based self-sensing control [9]

High-frequency sinusoidal flux linkage with 850 Hz frequency and amplitude of 7.5% of the magnet flux is superimposed on the corresponding MTPA flux linkage command, which achieves minimum losses during low-speed operation. Rotor position and speed are then estimated from the measured motor current.

The steady-state performance of the HFFI self-sensing technique on the designed motor is evaluated at a different speed and load conditions. Figure 19 compares the measured and estimated position.

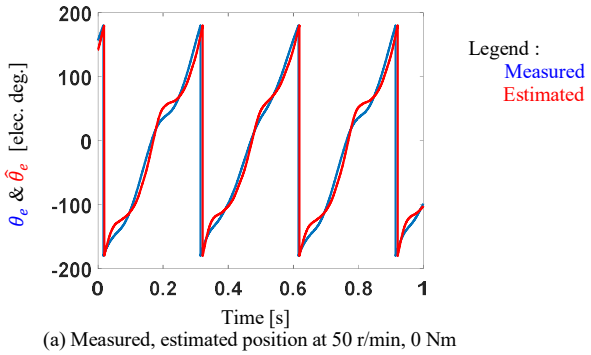

(a) Measured, estimated position at 50 r/min, 0 Nm

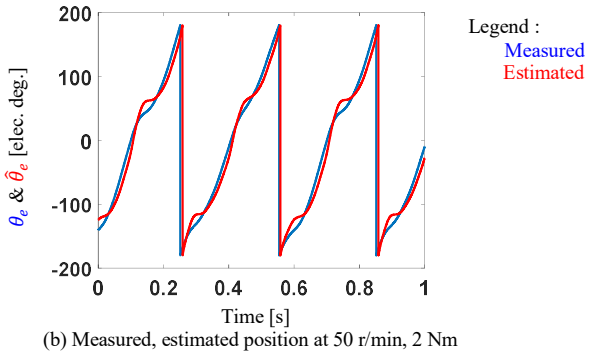

(b) Measured, estimated position at 50 r/min, 2 Nm

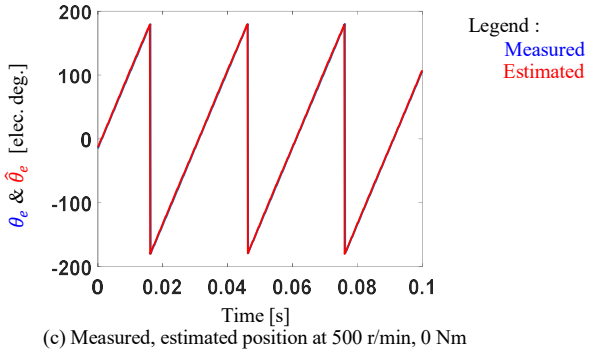

(c) Measured, estimated position at 500 r/min, 0 Nm

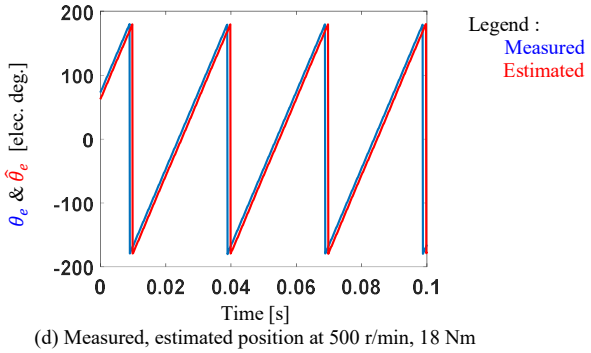

(d) Measured, estimated position at 500 r/min, 18 Nm

Fig. 19 Measured, estimated, position error when the designed motor is controlled using HFFI self-sensing DB-DTFC at different speed and load conditions

Oscillations in the estimated position showed up during the low-speed operation when the motor is run at 50 r/min, this is due to inverter non-linearity and dead-time effect (The used inverter has 3.5 μs dead-time). At this operating condition, the commanded voltage will be different from the actual one. As the

speed increases to 500 r/min, the inverter volt-sec error becomes negligible leading to lower error.

The designed motor was controlled using injection based self-sensing at 18 Nm which is more than the rated torque for this motor, which is typically unachievable with standard SPMSMs that have negligible saliency even at light load conditions. The position error is increased by 14 electrical degrees from the no load case to the rated torque case due to the cross-saturation effect and due to using fixed inductance values, this error can be easily compensated as described in [16].

V. Conclusions

In this paper, a methodology to design FW-SPMSMs for servo applications with enhanced self-sensing properties without degrading motor power conversion is presented.

The following conclusions can be reached from the results of this paper:

- Designing FW-SPMSM motors for servo applications with very low cogging and ripple torques can be achieved by shaping the magnet using bread-loaf or arc-shaped magnets to reduce airgap flux harmonics.
- Adding small iron notches between adjacent magnets improves the self-sensing properties by increasing q-axis inductance. However, they will slightly increase the leakage flux and will slightly affect the average motor torque.
- Adding d-axis flux barriers helps in saturating the d-axis flux path in the rotor which reduces d-axis inductance, creating a detectable saliency.
- The d-axis flux barriers also help in stabilizing the q-axis inductance with load variation. This is achieved by using the d-axis flux to saturate the q-axis flux path. In this case, the self-sensing performance of the motor will not degrade with load variations like standard FW-PM motors. The d-axis flux barriers also help reduce rotor mass and inertia, which improves motor dynamic performance.
- The designed FW-SPMSM for servo applications using the proposed design methodology was controlled using the injection-based self-sensing technique even at overload condition, due to the enhanced self-sensing properties of this motor.

Acknowledgment

The author wishes to acknowledge the motivation and support provided by the Wisconsin Electric Machines and Power Electronics Consortium (WEMPEC) of the University of Wisconsin-Madison, and Delta Electronics, Inc, Taiwan.2

References

[1] Sarikhani and O. A. Mohammed, "Sensorless Control of PM Synchronous Machines by Physics-Based EMF Observer," in *IEEE Transactions on Energy Conversion*, vol. 27, no. 4, pp. 1009-1017, Dec. 2012.

[2] Y. Zhao, W. Qiao and L. Wu, "Improved Rotor Position and Speed Estimators for Sensorless Control of Interior Permanent-Magnet Synchronous Machines," in IEEE Journal of Emerging and Selected Topics in Power Electronics, vol. 2, no. 3, pp. 627-639, Sept. 2014.

[3] S. K. Sul, Y. C. Kwon and Y. Lee, "Sensorless control of IPMSM for last 10 years and next 5 years," in CES Transactions on Electrical Machines and Systems, vol. 1, no. 2, pp. 91-99, 2017.

[4] A. Faggion, N. Bianchi and S. Bolognani, "Ringed-Pole Permanent-Magnet Synchronous Motor for Position Sensorless Drives," in *IEEE Transactions on Industry Applications*, vol. 47, no. 4, pp. 1759-1766, July-Aug. 2011.

[5] S. C. Yang, T. Suzuki, R. D. Lorenz, and T. M. Jahns, "Surface-permanentmagnet synchronous machine design for saliency-tracking self-sensing position estimation at zero and low speeds," IEEE Trans. Ind. Appl., vol. 47, no. 5, pp. 2103–2116, Sep./Oct. 2011.

[6] L. Alberti, N. Bianchi and S. Bolognani, "Comparison of different synchronous machines for sensorless drives," *IECON 2013 - 39th Annual Conference of the IEEE Industrial Electronics Society*, Vienna, 2013, pp. 8220-8226.

[7] Y. Kwon, J. Lee and S. Sul, "Full torque-range low-speed sensorless drive for heavily saturated IPMSMs by manipulation of convergence point," *2017 IEEE Energy Conversion Congress and Exposition (ECCE)*, Cincinnati, OH, 2017, pp. 865-872.

[8] H. M. Flieh, R. D. Lorenz, E. Totoki, S. Yamaguchi and Y. Nakamura, "Investigation of Different Servo Motor Designs for Servo Cycle Operations and Loss Minimizing Control Performance," in *IEEE Transactions on Industry Applications*, vol. 54, no. 6, pp. 5791-5801, Nov.-Dec. 2018.

[9] H. Flieh, T. Silininger, R. D. Lorenz, E. Totoki, " Self-Sensing via Flux Injection with Servo Dynamics including a Smooth Transition to Back-EMF Tracking," 2018 IEEE Energy Conversion Congress and Exposition, Portland, OR, 2018.

[10] G. R. Slemon, "On the design of high-performance surface-mounted PM motors," IEEE Trans. Ind. Appl., vol. 30, no. 1, pp. 134–140, Jan./Feb. 1994.

[11] D. C. Hanselman, Brushless Permanent-Magnet Motor Design, 1st ed. New York, NY, USA: McGraw-Hill, 1994.

[12] J. R. Hendershot and T. J. E. Miller, Design of Brushless PermanentMagnet Machines, 1st ed. Venice, FL, USA: Motor Design Books, 2010.

[13] T. A. Lipo, Introduction to AC Machine Design, 1st ed. Madison, WI, USA: Wisconsin Power Electron. Res. Center, Univ. Wisconsin, 2004.

[14] S. Ruangsinchaiwanich, Z. Q. Zhu, and D. Howe, "Influence of magnet shape on cogging torque and back-emf waveform in permanent magnet machines," in Proc. Int. Conf. Electr. Mach. Syst., vol. 1, 2005, pp. 284–289.

[15] Y. Li, Z. Q. Zhu, D. Howe, C. M. Bingham and D. A. Stone, "Improved Rotor-Position Estimation by Signal Injection in Brushless AC Motors, Accounting for Cross-Coupling Magnetic Saturation," in *IEEE Transactions on Industry Applications*, vol. 45, no. 5, pp. 1843-1850, Sept.-oct. 2009.